applied sciences

MDPI

Article

Development of Compact and Robust Physical System for Strontium Optical Lattice Clock

Yingxin Chen [1,2,3,†], Chihua Zhou [1,*,†], Wei Tan [1,2], Feng Guo [1], Guodong Zhao [1,3], Jian Xia [1], Junwei Meng [1] and Hong Chang [1,2,3,*]

[1] Key Laboratory of Time Reference and Application, National Time Service Center, Chinese Academy of Sciences, Xi'an 710600, China; chenyingxin@ntsc.ac.cn (Y.C.); tanwei@ntsc.ac.cn (W.T.); guofeng@ntsc.ac.cn (F.G.); zhaoguodong@ntsc.ac.cn (G.Z.); xiajian@ntsc.ac.cn (J.X.); mengjunwei@ntsc.ac.cn (J.M.)
[2] Hefei National Laboratory, Hefei 230088, China
[3] School of Astronomy and Space Science, University of Chinese Academy of Sciences, Beijing 100049, China
* Correspondence: zhouchihua@ntsc.ac.cn (C.Z.); changhong@ntsc.ac.cn (H.C.); Tel.: +86-029-8389085 (H.C.)
† These authors contributed equally to this work.

Abstract: Compact and robust optical clocks are significant in scientific research and engineering. Here, we present a physical system for a strontium atomic optical clock with dimensions of 465 mm × 588 mm × 415 mm and a weight of 66.6 kg. To date, this is one of the most compact physical systems ever reported. The application of the magnetic shielding box in this physical system allowed the effect of external magnetic field fluctuation on cold atoms to be negligible. The physical system passed rigorous environmental tests and remained operational. A wavelength meter integrated in this physical system could monitor the wavelengths of the incident laser, and it could automatically calibrate the wavelengths of all lasers using a microcomputer. This compact and robust physical system could be a hardware basis for demonstrating a portable optical clock or even a space optical clock.

Keywords: physical system; compact and robust; optical clock; strontium atoms

Citation: Chen, Y.; Zhou, C.; Tan, W.; Guo, F.; Zhao, G.; Xia, J.; Meng, J.; Chang, H. Development of Compact and Robust Physical System for Strontium Optical Lattice Clock. *Appl. Sci.* **2024**, *14*, 1551. https://doi.org/10.3390/app14041551

Received: 12 December 2023
Revised: 9 February 2024
Accepted: 10 February 2024
Published: 15 February 2024

1. Introduction

In recent years, there has been significant improvement in the stability and uncertainty of optical clocks, surpassing the performance of the current reference clock, i.e., the cesium microwave clock. Optical clocks demonstrate potential as the most promising candidate for the future redefinition of the second, based on optical transitions [1–10]. These clocks have found wide application in fundamental physics research. For instance, they have the potential to detect variations in the fine structure constant α [11–13] and have validated Einstein's general theory of relativity [14–17]. Furthermore, optical clocks have demonstrated significant potential in the field of geodesy [18,19], enabling the precise monitoring of various geological processes through the measurement of changes in gravitational potential, including magmatic activity, volcanic eruptions, post-seismic ground deformation, and solid Earth tides. Simultaneously, optical clocks possess the potential to play a key role in scientific research. In domains such as gravitational wave detection [20] and the exploration of dark matter [21–23], optical clocks are expected to play a significant role in the future. These applications help to establish a more comprehensive understanding of the fundamental laws of nature. However, due to their large size and complex structure, most high-performance optical clocks are limited to laboratory environments, restricting their broader application in precision tests of fundamental physics, chronometric-level geodesy, or high-precision navigation. Hence, the design and development of compact and robust optical clocks suitable for critical environments are of paramount importance.

Numerous research groups, both domestically and internationally, have delved into portable optical clocks [24–27]. For instance, in 2014, the European Laboratory for Non-Linear Spectroscopy (LENS) and the Physikalisch-Technische Bundesanstalt (PTB) cooperatively demonstrated the first transportable optical clock. The physical package of this optical clock had dimensions of 120 cm × 40 cm × 36 cm [28]. Subsequently, in 2017, PTB reported a new type of transportable optical clock housed in a trailer, with dimensions of 80 cm × 40 cm × 43 cm [29]. In 2018, the Heinrich-Heine-Universität Düsseldorf and PTB presented a compact optical lattice clock based on bosonic atoms, with a volume of 1 m^3 and an uncertainty of 2.0×10^{-17} [30]. In 2020, the National Time Service Center (NTSC) unveiled a compact optical clock, whose physical system had a volume of 0.3 m^2 [31]. RIKEN also developed a pair of transportable optical clocks in 2020 [32], encased within a magnetic shield box with a side length of approximately 60 cm [33]. More recently, the University of Birmingham presented a field-deployable atomics package designed for an optical lattice clock, which exhibited a remarkable volumetric size, occupying only 121 L, including the laser system. This development marked a significant step in the direction of highly portable optical clocks suitable for a wide range of applications [34]. Typically, after transporting a standard portable optical clock system from the laboratory to the working site, manual adjustments are made to restore the system to its optimal state. However, for specialized optical clocks, like those on space stations or satellites, manual readjustments may not be feasible. To withstand extreme vibration environments, a highly robust optical clock becomes imperative.

In this manuscript, we present a strontium optical clock physical system with a compact structure and exceptional environmental adaptability. Specific improvements include a robust and low-power atomic oven, a short Zeeman slower, a miniature magneto-optical trapping (MOT) vacuum chamber equipped with a magnetic shield, integrated optical setups, and a laser frequency locking system. To realize the stable operation of the physical system outside the laboratory, strengthening structural design was applied. The system had dimensions of 465 mm × 588 mm × 415 mm and a mass of 66.6 kg, making it one of the smallest optical clocks reported to date. Compared with complex laboratory optical clocks, the physical system described herein offers further practical applications.

To verify the physical system's adaptability to mechanical vibrations and temperature fluctuations, we conducted mechanical vibration tests and high–low temperature cycle tests. The results showed that the impact of mechanical vibrations and temperature fluctuations on the physical system is relatively limited, laying a robust foundation for conducting experiments in more challenging environments. Moreover, to ensure the steady operation of the physical system in environments with periodic fluctuations in the peripheral magnetic field, laboratory simulations were performed to analyze the impact of magnetic field variations on lattice loading. Consequently, a magnetic shield box, effectively attenuating substantial magnetic field fluctuations, was developed and installed to cover the MOT chamber. Additionally, to enable the automatic calibration of the attached lasers, a wavemeter was integrated into the system to monitor the wavelengths of all the lasers and facilitate automatic calibration.

2. The Compact and Robust Physical System

The upper floor of the physical system comprised a laser wavelength control system that included a structurally reinforced commercial wavemeter (High-Finesse, WS-7), a laser mode switcher, and a computer. The laser wavelength control system and the power supply for the vacuum pump were mounted on a liquid-cold plate. This plate could conduct heat away from the devices and act as a structural component, as shown in Figure 1. To display more details inside, the shells of the system are not shown. The laser wavelength control system could record the wavelengths of all the lasers in the optical clock system in real-time, and enable automatic laser frequency adjustment.

The physical package was located on the lower floor of the physical system. This physical package was highly compact and structurally designed and had dimensions of

280 mm × 588 mm × 415 mm, as shown in Figure 2. Two ion-gettering pumps were used to maintain the vacuum of the chamber, each consisting of a 100 L/s getter pump and a 5 L/s ion pump. Compared with high-speed ion pumps, this ion-gettering pump had a smaller volume and weight but allowed relatively high pumping speeds due to the presence of the getter. In order to reduce the influence of the background pressure on the atomic cooling and detection, we set up a differential pumping stage between the atomic oven and the MOT region. We employed a titanium alloy tube with a length of 160 mm and an inner diameter of 6 mm, which covers the section from the beginning of the Zeeman slower to the front of the MOT vacuum chamber center region. This effectively preserved the high vacuum condition of the MOT vacuum chamber and prevented the degradation of the vacuum environment by the atomic oven operating at a high temperature. When the optical clock operated normally (with an oven temperature of up to 400 °C), the pressure in the MOT vacuum chamber was under 1.3×10^{-9} Pa. Furthermore, the system's status under power-off conditions was also tested to simulate optical clocks operating outside the laboratory. Because the getter pumps could sustain the chamber vacuum during the power-off period, after a week of power failure, the chamber pressure could be returned to the normal level within approximately 6 h once power was restored.

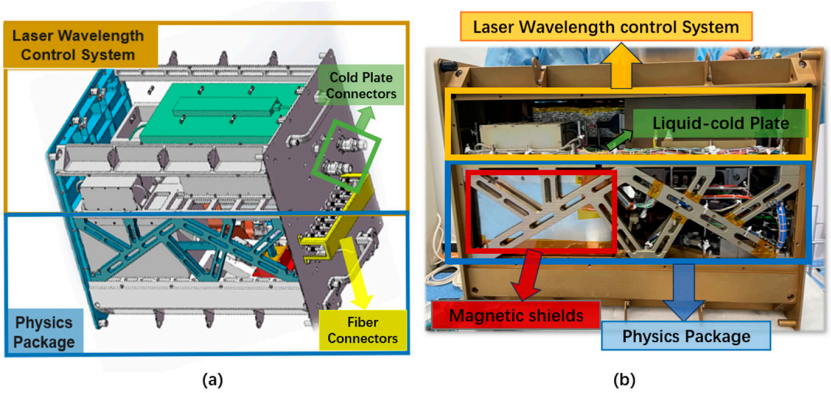

Figure 1. Physical system, design drawing (**a**), and real picture (**b**).

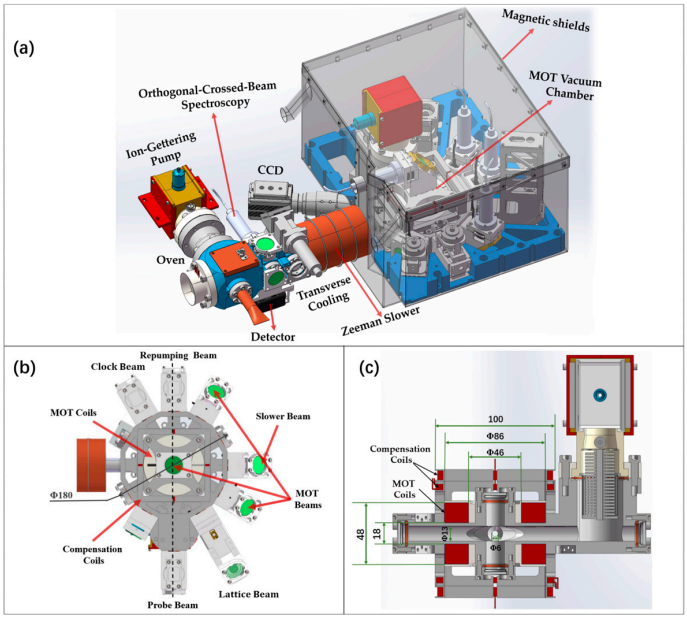

Figure 2. (**a**) Physics package design. (**b**) Top view of the MOT vacuum chamber. (**c**) Cross-sectional view of the MOT vacuum chamber, facing the atomic oven.

A high-efficiency oven based on heating inside the vacuum chamber was developed to reduce thermal dispersion from the heating wire to the environment. Furthermore, a multi-layer heat shield made of polished aluminum was placed around the heating filament perimeter to curb the heat loss caused by radiation. Through optimization, the power consumption of this oven was below 14 W during the experiment. To obtain a collimated atomic beam, approximately 50 stainless steel capillary collimators were positioned at the outlet of the oven. Each capillary had a length of 8 mm and a diameter of 0.2 mm, resulting in an emitted atomic beam with a divergence angle of approximately 25 mrad. However, this physical collimation could not ensure sufficient atoms entering the MOT vacuum chamber. Therefore, a two-dimensional transverse cooling vacuum chamber with four perpendicular CF 16 view plates was installed to further reduce the atomic beam divergence angle. There was another chamber beside the former vacuum chamber for detecting the fluorescence signals, allowing the primary cooling laser frequency (461 nm) to be locked onto the atomic transition $^1S_0 \rightarrow {}^1P_1$. This setup eliminated the need for an additional vacuum setup to lock the laser frequency.

Reducing the length of the Zeeman slower is an effective method to diminish the volume of the physical package. We measured the correlation between various slower lengths and the trapped low-velocity atoms in the Blue MOT. When the slower length was reduced to 10 cm, which is 1/3 of that in a traditional laboratory physical package, we still trapped nearly 3×10^6 ^{87}Sr atoms in the Blue MOT [35]. This result means that the short Zeeman slower could guarantee sufficient cold atoms in clock detection. Due to the shorter length of the slower, its weight and power consumption were also significantly reduced (mass of 3 kg, maximum power consumption of 19 W).

We designed and implemented a compact MOT vacuum chamber for atomic cooling and detection. The MOT vacuum chamber had 15 CF 16 viewports, distributed in different directions, to facilitate the connection and integration with other optical and mechanical components. In Figure 2b, the top view illustrates the layout of the lasers and magnetic field coils within the MOT region. To achieve a flat configuration, most windows were positioned on the horizontal plane, with only three vertical windows—two for the vertical MOT beam and one for the ion-gettering pump (located outside the MOT center region). The diameter of the vacuum chamber is only 180 mm, which has a very high space efficiency. To reduce atom adhesion, the window facing the oven was made of sapphire.

Figure 2c provides a cross-sectional view of the MOT vacuum chamber, cut along the black dashed line in Figure 2b, facing the atomic oven. The figure outlines the dimensions of the vacuum chamber, with a light pipe diameter of only 13 mm to reduce the distance between the anti-Helmholtz coils, achieving a high magnetic field gradient and low power consumption. The inner and outer diameters of the anti-Helmholtz coils are 46 mm and 86 mm, respectively, with minimum and maximum distances of 18 mm and 48 mm. At a current of 2 A, the magnetic field gradient at the MOT center reached 50 Gs/cm, accompanied by an average power consumption of only 6.8 W. No water cooling or heat sink was required, significantly simplifying the structure of the physical package. The compensation coils comprise three pairs of square coils, each with a side length of 100 mm. To reduce weight, the chamber was made of titanium alloy.

Because all lasers incident the physical system via optical fibers, we designed a set of integrated optical setups to adjust the alignment and polarization of the incident beam, as shown in Figure 3a. To maintain beam pointing stability, we designed threaded holes on the chamber shell of the physical package to install the integrated optical setups. Furthermore, all optical mirror mounts were springless and devoid of adjustable knobs. To enhance comprehension, we have provided a detailed explanation of the integrated optical setups using the probe beam optical setup as an example. In Figure 3b, an exploded view of the probe beam optical setup is presented, illustrating the configuration of the springless mirror mounts. The 461nm probe laser is coupled into a non-adjustable collimator (1) to collimate the beam. The collimated beam has a diameter of approximately 1 mm and passes through a half-wave plate (3) and a wedge prism (5), finally entering the MOT

vacuum chamber via a 45° mirror (9). The half-wave plate and wedge prism are mounted on rotation mounts (4), allowing the adjustment of the polarization and beam direction of the probe laser. After adjustment, they are secured in place using a support bracket (7). Due to the limited adjustment range of the wedge prism, high precision is required during mechanical machining. Additionally, a pedestal was designed on the mainframe (6), where the angle of the 45° mirror mount (11) is adjusted by adding aluminum alloy shims of varying thickness to ensure the alignment of the laser with the atomic position (no shims are used in our system). As the repumping beam enters from the opposite side of the probe beam, a 0° mirror mount (8) was added on the mainframe to ensure the repumping beam can return along the same path. To improve the anti-vibration capability of the system, we applied 2216-type epoxy adhesive to all screws for further reinforcement of the optical components.

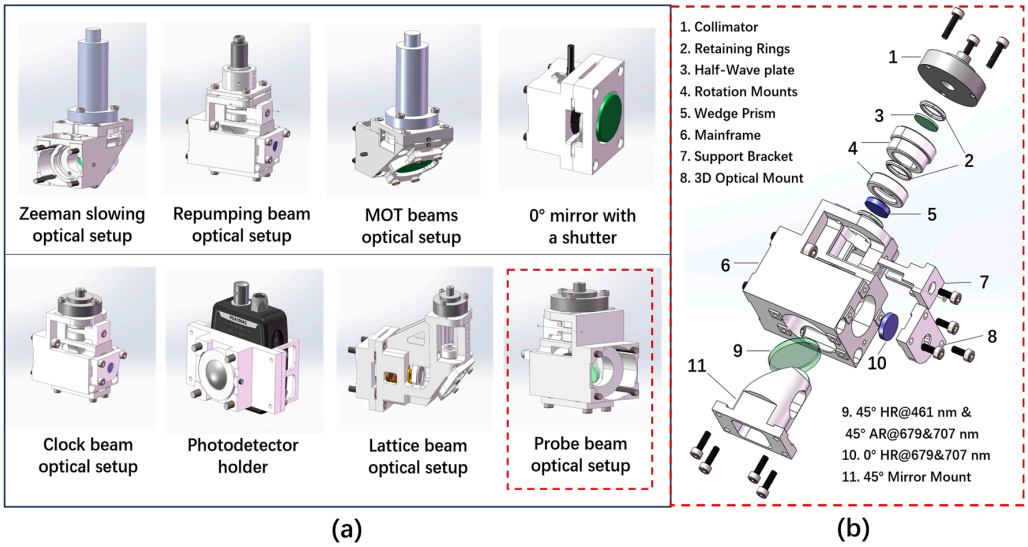

Figure 3. (**a**) Schematic of the customized integrated optical setups. (**b**) Exploded view of the probe beam optical setup.

Furthermore, to prevent the influence of complex magnetic field environments on the trapping and detection of atoms, we designed a magnetic shielding box made of permalloy. It measures 342 mm × 262 mm × 254 mm with a wall thickness of 1 mm. The shield was installed outside the MOT chamber, as shown in Figure 2a, and its shielding effectiveness was evaluated using a CH-hall Electronic Devices Company Model 3600 Gaussmeter. The results indicated an approximate 20 dB attenuation in the magnetic field strength at the center of the MOT chamber. Due to the structural design constraints, we cannot install the ion-gettering pump outside the magnetic shielding box. We measured the magnetic field generated by the ion-gettering pump in operation and found that its field strength was very weak. Moreover, the field was stable, and we could eliminate its interference with the clock detection by compensating the field. The effects of the magnetic shielding box on the optical clock experiment will be thoroughly discussed in the "environmental testing" section of this manuscript.

To reduce the weight of the physics package, mechanical analyses and iterative designs were conducted. The final frame support structure featured large area cutouts and stiffening ribs, as shown in Figure 4. The frame support structure was sustained by aluminum alloy support beams on both long sides to minimize elastic deformation. The physical package was connected to the cold plate through multiple side support beams to reinforce the rigidity of the entire physical system, as illustrated in Figure 1. In summary, engineered modifications have been applied to the physical package in terms of size, weight, power consumption, vacuum, magnetic field, and vibration resistance, making it applicable to a wider range of situations.

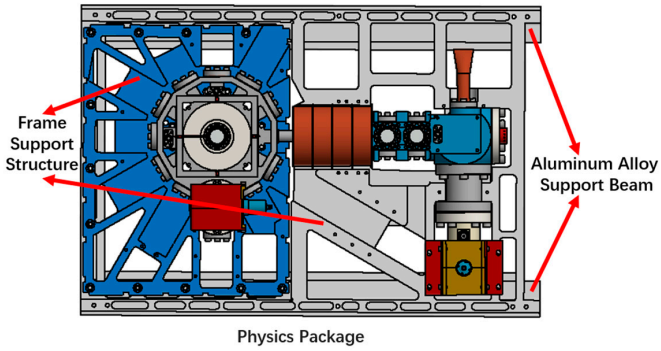

Figure 4. Support structure design of the physics package.

3. Operation and Results

Adjusting the laser wavelength to its operating point is a critical and primary step in operating an optical clock system. Traditionally, this process has been performed manually in optical clock experiments. However, in complex environments outside the laboratory, automating this process becomes necessary. We innovatively employed a wavemeter to achieve automatic and efficient laser wavelength optimization. The proposed methodology is illustrated schematically in Figure 5a. All lasers are linked to a wavemeter via a multichannel laser switch. Initially, software presets parameters for each laser, including temperature, current, and voltage. Subsequently, software-controlled iterations were conducted to explore parameter combinations, recording wavelength data every 500 ms. After completing iterations, multiple parameter combinations matching the target wavelength were identified based on the recorded wavelength data. Each laser's parameters were then sequentially adjusted to match these combinations. The internal piezoelectric ceramics (PZT) within the lasers were scanned to determine the parameter combination with the largest frequency tuning range, serving as the optimal configuration for the lasers. Leveraging a multichannel laser switch enabled simultaneous wavelength searches for all lasers, completing the process in under 5 min, surpassing manual operations in efficiency. This automated approach significantly enhances experimental efficiency, particularly in complex environments. Subsequently, based on the distinct frequency linewidth requirements of each laser, they were individually referenced to different frequency standards. Specifically, lasers operating at 689-nm, 698-nm were referenced to an ultra-high stability optical cavity; the 461-nm laser was referenced to the atomic transition $^1S_0 \rightarrow {}^1P_1$, while the 679-nm and 707-nm lasers underwent frequency calibration using the wavemeter. The 813nm laser was also referenced to the wavemeter since we did not have an ultra-stable cavity for 813-nm. We are considering the option of locking the 813-nm laser to a femtosecond optical frequency comb referenced to the 698-nm clock laser.

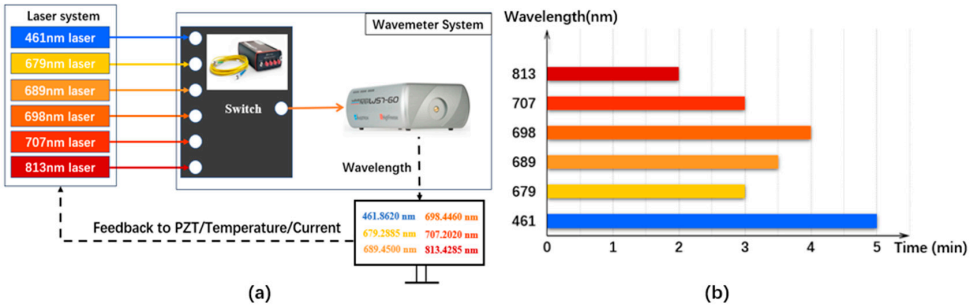

Figure 5. (**a**) Schematic of automatic laser wavelength searching; (**b**) time consumption.

Figure 6a illustrates the timing sequence for preparing cold atoms. Initially, primary cooling was conducted, where the atomic beam was pre-slowed using the slower beam with a power of 30 mW and a beam radius of 4 mm. Subsequently, employing the combined

effect of the MOT beams (with a single-beam power of 6 mW and a beam radius of 4 mm), repumping beam (where the 707-nm laser had a power of approximately 8 mW and the 679-nm laser had a power of approximately 4 mW, both with a beam radius of 4 mm), and a gradient magnetic field over a duration of 550 ms, up to 3×10^6 ^{87}Sr atoms were loaded into the Blue MOT, achieving a temperature of approximately 5 mK. Throughout this phase, the magnetic field gradient remained at 50 Gs/cm. The transfer of atoms from the Blue MOT to the Red MOT took place in two phases. The first phase was a Broadband Red MOT, where each beam of the 689-nm MOT lasers operated at a power of approximately 3 mW, and each stirring laser operated at a power of approximately 0.8 mW. The beam radius for both lasers was set at 4 mm. Simultaneously, an acousto-optic modulator (AOM) widened the 689-nm laser linewidth to around 2 MHz, with a modulation frequency of around 40 kHz. It is noteworthy that we optimized spatial efficiency and system reliability by utilizing a Fiber Array from Evanescent Optics. This Fiber Array, measuring only $12.5 \times 10 \times 1.3$ cm^3, was used to combine Blue MOT, Red MOT, and stirring lasers and was split into three outputs for the MOT beams. Concurrently, the magnetic field gradient decreased to 3 Gs/cm and held for 10 ms, followed by a linear increase to 10 Gs/cm over the subsequent 90 ms to ensure a sufficient atom transfer to the Red MOT. The second phase involved a single-frequency Red MOT, deactivating the modulation of the 689-nm laser and reducing its power. The power of each beam of the 689-nm Red MOT lasers was adjusted to 0.8 mW, and the stirring laser's power was diminished to 50 µW. After 60 ms, we achieved a Red MOT with a temperature of approximately 4.5 µK and a population of about 2.8×10^5. Subsequently, all optical and magnetic fields, excluding the 813-nm lattice beam (maintained in an active state), were turned off to load the atoms into a one-dimensional optical lattice. The lattice beam operated at a power of 500 mW, a waist radius of 53 µm, and a trap depth of approximately 92 Er (Er = 3.44 kHz, representing the recoil energy). Eventually, around 1.4×10^4 ^{87}Sr atoms were transferred from the Red MOT to the lattice. The images captured by the CCD for the Blue MOT, Red MOT, and atoms in the optical lattice are, respectively, presented in Figure 6b. By analyzing the decay of atoms trapped in a lattice, we estimated their lifetime to be approximately 3.6 s, as illustrated in Figure 6c. The lattice lifetime of transportable optical clocks typically ranges from several hundred milliseconds to a few seconds [30,31,34,36], and our lattice lifetime is comparable to that of other transportable optical clocks. However, there is a notable difference when compared to laboratory clocks, where the lattice lifetime of optical clocks often extends to several seconds to tens of seconds [37]. We attribute this discrepancy primarily to the lack of active power stabilization on the lattice laser, which leads to significant power noise and consequently impacts the lattice lifetime. Nonetheless, given that our lattice lifetime is already sufficiently long, we have not pursued further investigation into the impact of power noise on the lattice lifetime.

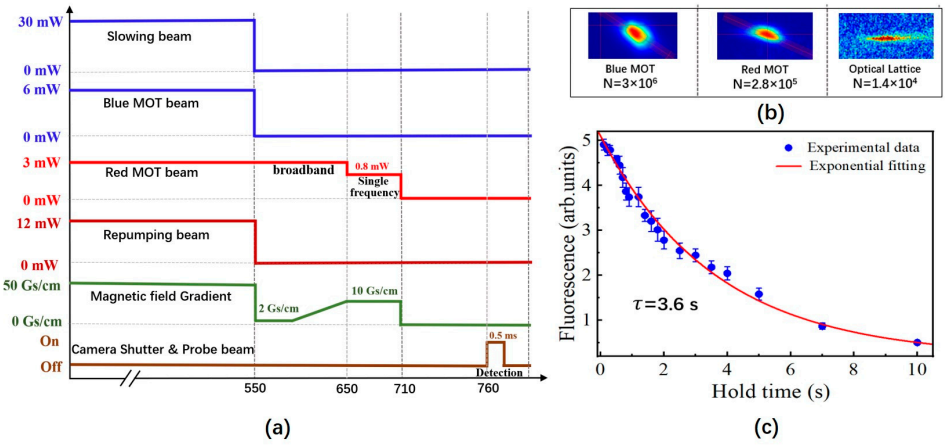

Figure 6. (**a**) The timing sequence in the Sr optical clock; (**b**) images recorded in situ for Blue MOT, Red MOT, and atoms in lattice; (**c**) the lattice lifetime measurement.

4. Environmental Testing

To extend the application of optical clocks to as many scenarios as possible, it is imperative to address the challenges posed by the complex and dynamic environmental conditions outside the laboratory. Therefore, we conducted exhaustive evaluations to determine the adaptability of the physical system in magnetic, mechanical, and temperature environments.

4.1. Magnetic Shielding

Magnetic field fluctuations pose a significant challenge to optical clocks operating in mobile platforms, e.g., satellites, space stations, planes, or trucks. Notably, as satellites or space stations orbit the Earth, the surrounding geomagnetic field undergoes changes owing to their motion. The magnitude of these variations can exceed 80 μT, significantly impacting the normal operation of onboard optical clocks [38].

Theoretical analysis regarding the impact of geomagnetic field changes on strontium optical clocks indicates that, to prevent disruption to lattice loading, the amplitude of magnetic field changes must be less than 10 μT. Additionally, for a space optical clock targeting stability and a frequency uncertainty of 5×10^{-17}, magnetic field fluctuations between adjacent interrogation cycles of the clock should be less than 3 nT/s. To comprehensively understand the impact of magnetic field variations on strontium optical clocks, we introduced equivalent external magnetic field changes and observed in experiments how such fluctuations led to the instability of atoms loaded into the optical lattice [39].

Hence, optical clocks that frequently operate outside laboratories must feature the capability for magnetic field compensation or shielding. In comparison to magnetic field compensation, shielding against various environmental challenges might be a preferable option. As described in the manuscript's second section, we installed a magnetic shielding box outside the MOT chamber. Upon testing, this shield attenuated the magnetic field by approximately 20 dB at its center. This implies that the maximum fluctuation of the magnetic field in the space station orbit can be reduced to 0.6 μT. Consequently, the maximum rate of change would be 0.22 nT/s, which is significantly lower than the theoretical values of 10 μT and 3 nT/s.

Finally, we experimentally evaluated the effectiveness of the magnetic shielding box in mitigating external magnetic field fluctuations. According to an investigation report by the International Geomagnetic Reference Field (IGRF), the magnetic field intensity in the space station's orbit is comparable to that on Earth's surface. Therefore, to simplify the experimental conditions, we opted to simulate the space station's magnetic field changes by rotating the physical system on the ground. The experimental results, depicted in Figure 7, exhibit slight changes in the number and images of lattice atoms recorded by a CCD camera after rotating the physical system by 180° on the ground. This demonstrates that the magnetic shielding box enables the physical system to withstand extremely challenging magnetic field environments, thus opening up broader possibilities for optical clock applications.

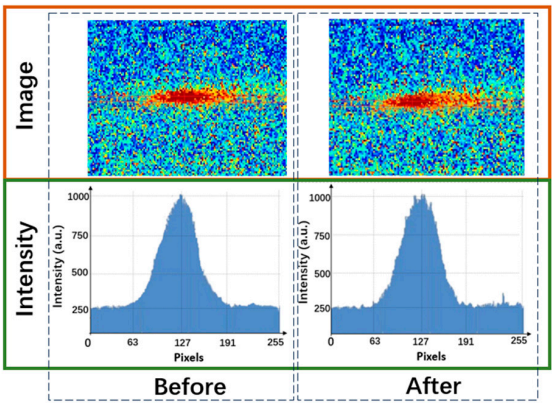

Figure 7. Images of lattice atoms before and after magnetic field alteration in the presence of the magnetic shielding box.

4.2. Mechanical and Thermal Environments

During transportation outside the laboratory, optical clocks must endure harsh transport conditions, including the road, the sea, and even a rocket. To ensure that the system can work normally without manual adjustment after transportation, especially for mechanical structure adjustments, environmental testing is necessary to verify the adaptability of the system to various mechanical and thermal environments.

Figure 8 illustrates the thermal test temperature curve of a temperature chamber calibrated by the Institute of Metrology Science. The test conditions were set according to the experimental payload requirements for the Chinese space station, encompassing the following: (1) a temperature range from +10 °C to +40 °C; (2) both high and low temperature holding times of 4 h; (3) temperature change rates averaging 3 °C /min to 5 °C /min; (4) a total of 12 cycles; (5) atmospheric pressure set to normal conditions.

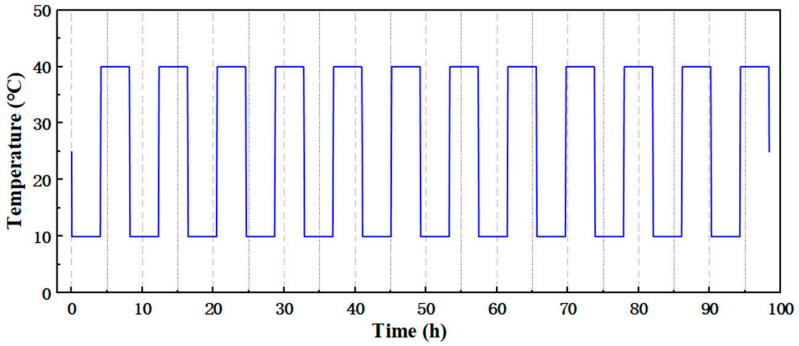

Figure 8. Thermal test conditions. High temperature is 40 °C, low temperature is 10 °C, each cycle is 8 h, total of 12 cycles.

Tables 1 and 2 outline the test conditions for the sinusoidal swept-frequency vibration and random vibration tests, respectively. These conditions were established based on the experimental payload requirements for the Chinese space station. All equipment, including vibration tables, experimental testing equipment, and the sensors used in both test types, underwent calibration and certification by third-party metrology.

Table 1. Test conditions for sinusoidal swept-frequency vibration.

Parameter Name	Parameter Value			
	Frequency Range (Hz)			
	4–10	**10–17**	**17–40**	**40–100**
Amplitude 0~P	5 mm	2 g	3.4 g	2 g
Load Scan Rate	4 oct/min			
Load Direction	Three Axial Directions			

Table 2. Test conditions for random vibration.

Parameter Name	Parameter Value		
	Frequency Range (Hz)		
	10–50	**50–300**	**300–2000**
Power spectrum density (PSD)	3 dB/oct	0.0049 g^2/Hz	−12 dB/oct
Total Root Mean Square Acceleration (RMSA)	2.14 grms		
Duration of Each Experiment	60 s		
Load Direction	Three Axial Directions		

The fundamental frequency of the physical system was determined through feature-level sweeping in three directions. The fundamental frequencies in the X, Y, and Z directions

were measured at 49, 75, and 49 Hz, respectively, meeting the requirement that the designed fundamental frequency of the experimental payload should exceed 40 Hz. As illustrated in Figure 9 (left), the swept frequency response curve of the physical system in the Z direction at an eigenlevel of 0.2 g is presented. Figure 9 (middle, right) illustrate the sinusoidal and random response curves of the physical system, respectively. The response outcomes from both tests are deemed satisfactory. It is worth noting that, for the sake of visual clarity, Figure 9 exclusively showcases the test results along the Z-axis.

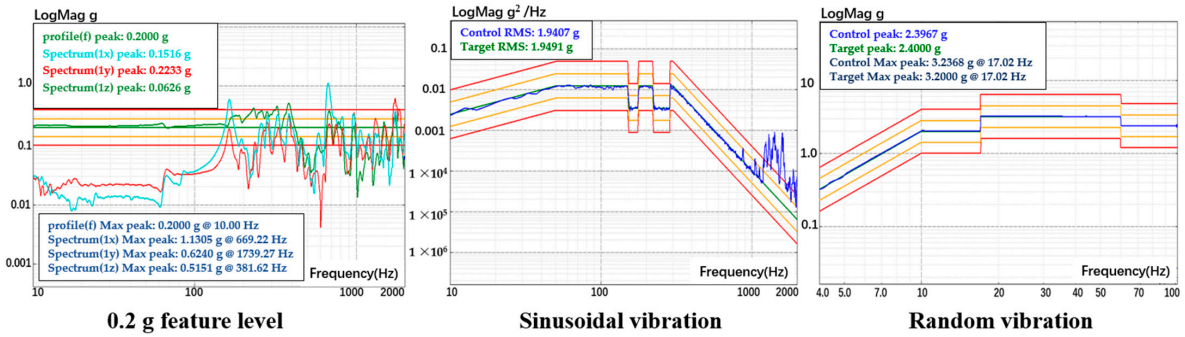

Figure 9. Vibration tests. From left to right are the sweep curves of the 0.2 g characteristic level, sinusoidal vibration, and random vibration test control curves in the Z direction, respectively.

After conducting the environmental tests, we proceeded with an electrical power-up test on the physical system. The vacuum of the chambers was meticulously examined and found to be identical to its pre-test state, confirming the effectiveness of the construction and support structure within the physical system. Among the system components, the lattice laser demands the strictest beam alignment, and lattice confinement denotes the final phase of cold atom capture. Hence, demonstrating that the environmental tests did not impact lattice loading serves to validate the safety and reliability of our custom integrated optical setup and its fixation method.

Figure 10 illustrates images of the Blue MOT and lattice atoms before and after the environmental tests. The Blue MOT image remained nearly unchanged, with the atom population staying constant at approximately 3×10^6 before and after the tests. However, we observed a slight alteration in the shape of lattice atoms, with the population of atoms within the lattice reducing from 1.4×10^4 to 1.2×10^4, likely due to the 2216 epoxy adhesive on the screws not having fully solidified during the environmental tests. To ensure the reliability of the system, we conducted several additional environmental tests, revealing no further changes in the shape or quantity of lattice atoms. Moreover, transporting the physical system from Xi'an to various locations like Changsha, Beijing, Tianjin, and Hainan via vehicles, trains, and ships revealed encouraging results, with the system's performance remaining intact after transportation.

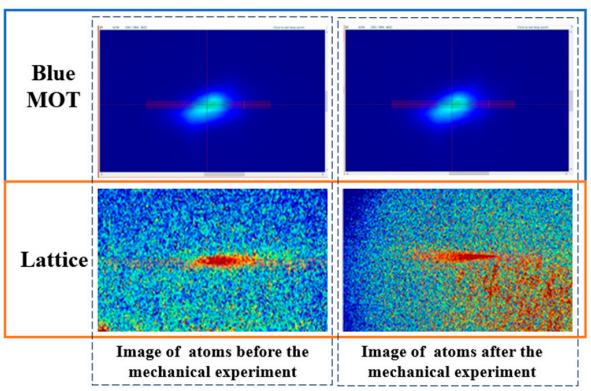

Figure 10. Images of atoms before and after the environmental tests.

5. Conclusions

In summary, we have developed a compact, lightweight, and robust physical system for a strontium optical lattice clock, making it well suited for operation outside laboratory conditions. With dimensions of 465 mm × 588 mm × 415 mm, a mass of 66.6 kg, and a total power consumption of less than 60 W (40 W for the physics package and 20 W for the wavelength control system), it stands as one of the most compact physical systems of its kind reported to date. The system operates automatically without requiring manual assistance, typically locking all lasers within 5 min. Using this system, we successfully loaded 1.4×10^4 ^{87}Sr atoms into 1D optical lattices with an estimated lifetime of 3.6 s.

Additionally, we conducted numerous environmental tests. Despite undergoing multiple intercity relocations (including road, rail, and sea transportation), prolonged power outage tests, mechanical tests, thermal tests, and a series of harsh conditions, the performance of the physical system remained stable. The use of the magnetic shielding box allowed the physical system to rotate on the ground while maintaining atom capture and detection.

Through various engineering designs, the physical system proved to be suitable for conditions outside the laboratory due to its size, power consumption, quality, and reliability. This advancement can accelerate the development of transportable optical clocks, and even space optical clocks, facilitating their use for experiments in outdoor environments or outer space. It bears significant implications for fundamental physics research, navigation systems, quantum science, and related fields [40].

Author Contributions: Conceptualization, Y.C. and C.Z.; methodology, Y.C., W.T. and C.Z.; software, J.X., G.Z. and F.G.; validation, Y.C., C.Z., W.T. and J.M.; formal analysis, Y.C., W.T. and C.Z.; writing—original draft preparation, Y.C. and C.Z.; writing—review and editing, C.Z. and H.C.; supervision, H.C.; project administration, H.C. All authors have read and agreed to the published version of the manuscript.

Funding: This research received no external funding.

Institutional Review Board Statement: Not applicable.

Informed Consent Statement: Not applicable.

Data Availability Statement: Data are contained within the article.

Conflicts of Interest: The authors declare no conflicts of interest.

References

1. Taylor, B.N.; Mohr, P.J. The Role of Fundamental Constants in the International System of Units (SI): Present and Future. *IEEE Trans. Instrum. Meas.* **2001**, *50*, 563–567. [CrossRef]
2. Swallows, M.D.; Bishof, M.; Lin, Y.; Blatt, S.; Martin, M.J.; Rey, A.M.; Ye, J. Suppression of Collisional Shifts in a Strongly Interacting Lattice Clock. *Science* **2011**, *331*, 1043–1046. [CrossRef]
3. Le Targat, R.; Lorini, L.; Le Coq, Y.; Zawada, M.; Guéna, J.; Abgrall, M.; Gurov, M.; Rosenbusch, P.; Rovera, D.G.; Nagórny, B.; et al. Experimental Realization of an Optical Second with Strontium Lattice Clocks. *Nat. Commun.* **2013**, *4*, 210. [CrossRef]
4. Nicholson, T.L.; Campbell, S.L.; Hutson, R.B.; Marti, G.E.; Bloom, B.J.; McNally, R.L.; Zhang, W.; Barrett, M.D.; Safronova, M.S.; Strouse, G.F.; et al. Systematic Evaluation of an Atomic Clock at 2×10^{-18} Total Uncertainty. *Nat. Commun.* **2015**, *6*, 6896. [CrossRef]
5. Huntemann, N.; Sanner, C.; Lipphardt, B.; Tamm, C.; Peik, E. Single-Ion Atomic Clock with 3×10^{-18} Systematic Uncertainty. *Phys. Rev. Lett.* **2016**, *116*, 063001. [CrossRef]
6. McGrew, W.F.; Zhang, X.; Fasano, R.J.; Schäffer, S.A.; Beloy, K.; Nicolodi, D.; Brown, R.C.; Hinkley, N.; Milani, G.; Schioppo, M.; et al. Atomic Clock Performance Enabling Geodesy below the Centimetre Level. *Nature* **2018**, *564*, 87–90. [CrossRef]
7. Riehle, F.; Gill, P.; Arias, F.; Robertsson, L. The CIPM List of Recommended Frequency Standard Values: Guidelines and Procedures. *Metrologia* **2018**, *55*, 188–200. [CrossRef]
8. Sanner, C.; Huntemann, N.; Lange, R.; Tamm, C.; Peik, E.; Safronova, M.S.; Porsev, S.G. Optical Clock Comparison for Lorentz Symmetry Testing. *Nature* **2019**, *567*, 204–220. [CrossRef] [PubMed]
9. Brewer, S.M.; Chen, J.-S.; Hankin, A.M.; Clements, E.R.; Chou, C.W.; Wineland, D.J.; Hume, D.B.; Leibrandt, D.R. An $^{27}Al^+$ quantum-logic clock with systematic uncertainty below 10^{-18}. *Phys. Rev. Lett.* **2019**, *123*, 033201. [CrossRef] [PubMed]
10. Zhang, J.; Shi, T.; Miao, J.; Chen, J. The Development of Active Optical Clock. *AAPPS Bull.* **2023**, *33*, 10. [CrossRef]

11. Huntemann, N.; Lipphardt, B.; Tamm, C.; Gerginov, V.; Weyers, S.; Peik, E. Improved Limit on a Temporal Variation of Mp/Me from Comparisons of Yb^+ and Cs Atomic Clocks. *Phys. Rev. Lett.* **2014**, *113*, 210802. [CrossRef]
12. Godun, R.M.; Nisbet-Jones, P.B.R.; Jones, J.M.; King, S.A.; Johnson, L.A.M.; Margolis, H.S.; Szymaniec, K.; Lea, S.N.; Bongs, K.; Gill, P. Frequency Ratio of Two Optical Clock Transitions in $^{171}Yb^+$ and Constraints on the Time Variation of Fundamental Constants. *Phys. Rev. Lett.* **2014**, *113*, 210801. [CrossRef]
13. Ludlow, A.D.; Boyd, M.M.; Ye, J.; Peik, E.; Schmidt, P.O. Optical Atomic Clocks. *Rev. Mod. Phys.* **2015**, *87*, 637–701. [CrossRef]
14. Walsh, D.; Carswell, R.; Weymann, R. Twin Quasitellar Objects or Gravitational Lens. *Nature* **1979**, *279*, 381–384.
15. Chou, C.W.; Hume, D.B.; Rosenband, T.; Wineland, D.J. Optical Clocks and Relativity. *Science* **2010**, *329*, 1630–1633. [CrossRef] [PubMed]
16. Will, C.M. The Confrontation between General Relativity and Experiment. *Living Rev. Relativ.* **2006**, *9*, 3. [CrossRef] [PubMed]
17. Bongs, K.; Singh, Y. Earth-Based Clocks Test General Relativity. *Nat. Photonics* **2020**, *14*, 408–409. [CrossRef]
18. Bondarescu, R.; Schaerer, A.; Lundgren, A.; Hetenyi, G.; Houlie, N.; Jetzer, P.; Bondarescu, M. Ground-Based Optical Atomic Clocks as a Tool to Monitor Vertical Surface Motion. *Geophys. J. Int.* **2015**, *202*, 1770–1774. [CrossRef]
19. Tanaka, Y.; Katori, H. Exploring Potential Applications of Optical Lattice Clocks in a Plate Subduction Zone. *J. Geod.* **2021**, *95*, 93. [CrossRef]
20. Kolkowitz, S.; Pikovski, I.; Langellier, N.; Lukin, M.D.; Walsworth, R.L.; Ye, J. Gravitational Wave Detection with Optical Lattice Atomic Clocks. *Phys. Rev. D* **2016**, *94*, 124043. [CrossRef]
21. Derevianko, A.; Pospelov, M. Hunting for Topological Dark Matter with Atomic Clocks. *Nat. Phys.* **2014**, *10*, 933–936. [CrossRef]
22. Roberts, B.M.; Blewitt, G.; Dailey, C.; Murphy, M.; Pospelov, M.; Rollings, A.; Sherman, J.; Williams, W.; Derevianko, A. Search for Domain Wall Dark Matter with Atomic Clocks on Board Global Positioning System Satellites. *Nat. Commun.* **2017**, *8*, 1195. [CrossRef]
23. Wcislo, P.; Ablewski, P.; Beloy, K.; Bilicki, S.; Bober, M.; Brown, R.; Fasano, R.; Ciurylo, R.; Hachisu, H.; Ido, T.; et al. New Bounds on Dark Matter Coupling from a Global Network of Optical Atomic Clocks. *Sci. Adv.* **2018**, *4*, eaau4869. [CrossRef] [PubMed]
24. Cacciapuoti, L.; Dimarcq, N.; Santarelli, G.; Laurent, P.; Lemonde, P.; Clairon, A.; Berthoud, P.; Jornod, A.; Reina, F.; Feltham, S.; et al. Atomic Clock Ensemble in Space: Scientific Objectives and Mission Status. *Nucl. Phys. B-Proc. Suppl.* **2007**, *166*, 303–306. [CrossRef]
25. Schiller, S.; Görlitz, A.; Nevsky, A.; Koelemeij, J.C.J.; Wicht, A.; Gill, P.; Klein, H.A.; Margolis, H.S.; Mileti, G.; Sterr, U.; et al. Optical Clocks in Space. *Nucl. Phys. B-Proc. Suppl.* **2007**, *166*, 300–302. [CrossRef]
26. Grotti, J.; Koller, S.; Vogt, S.; Häfner, S.; Sterr, U.; Lisdat, C.; Denker, H.; Voigt, C.; Timmen, L.; Rolland, A.; et al. Geodesy and Metrology with a Transportable Optical Clock. *Nat. Phys.* **2018**, *14*, 437–441. [CrossRef]
27. Cao, J.; Zhang, P.; Shang, J.; Cui, K.; Yuan, J.; Chao, S.; Wang, S.; Shu, H.; Huang, X. A Compact, Transportable Single-Ion Optical Clock with 7.8×10^{-17} Systematic Uncertainty. *Appl. Phys. B* **2017**, *123*, 112. [CrossRef]
28. Poli, N.; Schioppo, M.; Vogt, S.; Falke, S.; Sterr, U.; Lisdat, C.; Tino, G.M. A Transportable Strontium Optical Lattice Clock. *Appl. Phys. B* **2014**, *117*, 1107–1116. [CrossRef]
29. Koller, S.B.; Grotti, J.; Vogt, S.; Al-Masoudi, A.; Dörscher, S.; Häfner, S.; Sterr, U.; Lisdat, C. Transportable Optical Lattice Clock with 7×10^{-17} Uncertainty. *Phys. Rev. Lett.* **2017**, *118*, 073601. [CrossRef]
30. Origlia, S.; Pramod, M.S.; Schiller, S.; Singh, Y.; Bongs, K.; Schwarz, R.; Al-Masoudi, A.; Dörscher, S.; Herbers, S.; Häfner, S.; et al. Towards an Optical Clock for Space: Compact, High-Performance Optical Lattice Clock Based on Bosonic Atoms. *Phys. Rev. A* **2018**, *98*, 053443. [CrossRef]
31. Kong, D.-H.; Wang, Z.-H.; Guo, F.; Zhang, Q.; Lu, X.-T.; Wang, Y.-B.; Chang, H. A Transportable Optical Lattice Clock at the National Time Service Center. *Chin. Phys. B* **2020**, *29*, 070602. [CrossRef]
32. Takamoto, M.; Ushijima, I.; Ohmae, N.; Yahagi, T.; Kokado, K.; Shinkai, H.; Katori, H. Test of General Relativity by a Pair of Transportable Optical Lattice Clocks. *Nat. Photonics* **2020**, *14*, 411–415. [CrossRef]
33. Ohmae, N.; Takamoto, M.; Takahashi, Y.; Kokubun, M.; Araki, K.; Hinton, A.; Ushijima, I.; Muramatsu, T.; Furumiya, T.; Sakai, Y.; et al. Transportable Strontium Optical Lattice Clocks Operated Outside Laboratory at the Level of 10^{-18} Uncertainty. *Adv. Quantum Technol* **2021**, *4*, 2100015. [CrossRef]
34. Kale, Y.B.; Singh, A.; Gellesch, M.; Jones, J.M.; Morris, D.; Aldous, M.; Bongs, K.; Singh, Y. Field Deployable Atomics Package for an Optical Lattice Clock. *Quantum Sci. Technol.* **2022**, *7*, 045004. [CrossRef]
35. Zhao, F.-J.; Gao, F.; Han, J.-X.; Zhou, C.-H.; Meng, J.-W.; Wang, Y.-B.; Guo, Y.; Zhang, S.-G.; Chang, H. Miniaturization of Physics System in Sr Optical Clock. *Acta Phys. Sin.* **2018**, *67*, 050601. [CrossRef]
36. Kock, O.; He, W.; Świerad, D.; Smith, L.; Hughes, J.; Bongs, K.; Singh, Y. Laser Controlled Atom Source for Optical Clocks. *Sci. Rep.* **2016**, *6*, 37321. [CrossRef] [PubMed]
37. Barbiero, M.; Calonico, D.; Levi, F.; Tarallo, M.G. Optically Loaded Strontium Lattice Clock With a Single Multi-Wavelength Reference Cavity. *IEEE Trans. Instrum. Meas.* **2022**, *71*, 1–9. [CrossRef]
38. Li, L.; Ji, J.-W.; Ren, W.; Zhao, X.; Peng, X.-K.; Xiang, J.-F.; Lv, D.-S.; Liu, L. Automatic compensation of magnetic field for a rubidium space cold atom clock. *Chin. Phys. B* **2016**, *25*, 073201. [CrossRef]

39. Ren, J.; Tan, W.; Guo, F.; Liu, H.; Chang, H. Magnetic Field Analysis and Active Compensation System for Strontium Optical Lattice Clock in Space. *Opt. Precis. Eng.* **2022**, *30*, 1337–1343. [CrossRef]
40. Hofstetter, W.; Qin, T. Quantum Simulation of Strongly Correlated Condensed Matter Systems. *J. Phys. B-At. Mol. Opt. Phys.* **2018**, *51*, 082001. [CrossRef]